Probing Surface and Bulk Electrochemical Processes on the $LaAlO_3$—$SrTiO_3$ Interface

Amit Kumar,[†] Thomas M. Arruda,[†] Yunseok Kim,[†] Ilia N. Ivanov,[†] Stephen Jesse,[†] Chung W. Bark,[‡] Nicholas C. Bristowe,[§] Emilio Artacho,[§,⊥,∥] Peter B. Littlewood,[§,¶] Chang-Beom Eom,[‡] and Sergei V. Kalinin[†,*]

[†]Center for Nanophase Materials Sciences, Oak Ridge National Laboratory, Oak Ridge, Tennessee 37831, United States, [‡]Department of Materials Science and Engineering, University of Wisconsin—Madison, Madison, Wisconsin 53706, United States, [§]Theory of Condensed Matter, Cavendish Laboratory, University of Cambridge, Cambridge CB3 0HE, United Kingdom, [⊥]CIC Nanogune Consolider and DIPC, Tolosa Hiribidea 76, 20018 San Sebastian, Spain, [∥]Basque Foundation for Science Ikerbasque, 48011 Bilbao, Spain, and [¶]Physical Sciences and Engineering, Argonne National Laboratory, Argonne, Illinois 60439, United States

ABSTRACT

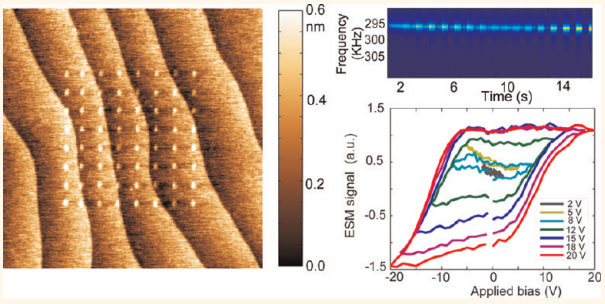

Local electrochemical phenomena on the surfaces of the $LaAlO_3$—$SrTiO_3$ heterostructure are explored using unipolar and bipolar dynamic electrochemical strain microscopy (D-ESM). The D-ESM suggests the presence of at least two distinct electrochemical processes, including fast reversible low-voltage process and slow high-voltage process. The latter process is associated with static surface deformations in the sub-nanometer regime. These behaviors are compared with Kelvin probe force microscopy hysteresis data. The possible origins of observed phenomena are discussed, and these studies suggest that charge-writing behavior in LAO—STO includes a strong surface/bulk electrochemical component and is more complicated than simple screening by surface adsorbates.

KEYWORDS: electrochemical · dynamic strain · microscopy · charge writing

The recent discovery of high-mobility 2D electron gas (2DEG) on the $LaAlO_3$—$SrTiO_3$ (LAO—STO) interface[1] has attracted much interest to this system. Following the initial discovery, field-controlled ground states were explored[2,3] and giant capacitance enhancement was discovered.[4] Since then, a broad variety of exotic physical phenomena including superconductivity,[5] magnetoresistance,[6] and magnetic regions[7] were observed. Further interest in these materials was attracted by the possibility of charge writing[8] that allows selective patterning of conductive and insulating regions, opening pathways to the fabrication of sub-10 nm oxide electronic devices.

This plethora of novel electronic phenomena has stimulated extensive efforts toward the understanding of the associated underpinning mechanisms. The prototypical *physical* mechanism suggested for interpretation of thickness-dependent electronic phenomena in LAO—STO is polar catastrophe,[9] that is, the transition of surface electrons to the interface at a certain critical thickness and the formation of an interface charge layer. This process can be strongly affected by lattice polarization,[10—12] and transferred electrons can be localized in multiple subbands.[13,14] The alternative mechanism for 2DEG formation is *chemical* cationic intermixing at the interfaces, that is, formation of metallic La-doped $SrTiO_3$.[15,16] Finally, a number of authors consider the formation of oxygen vacancies[17—21] on the LAO surface or segregating on the bulk as the inherent part of the process. A recent overview of the structure and properties of the LAO—STO system is given by Chambers *et al.*[22]

Mechanisms of metal—insulator transitions at the LAO—STO interface are of particular interest in the context of local SPM-based manipulation of local conductivity. Recently, a number of experimental studies have elucidated the role of charged surface adsorbates (water cycle mechanisms) on LAO—STO switching.[23—25] Notably, the presence of polar adsorbates on oxide surfaces[26—28] and coupling to, for example, ferroelectric state stability[29—31] and polarization dynamics[32,33] are well-recognized now, providing a broader context for this model. A recent theoretical effort by Bristowe *et al.*[34] analyzed the dynamic formation of *surface* vacancies as a mechanism for charge writing and

* Address correspondence to sergei2@ornl.gov.

Received for review December 19, 2011 and accepted April 10, 2012.

Published online April 10, 2012
10.1021/nn204960c

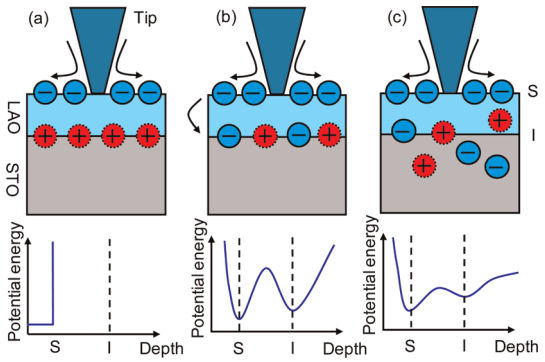

Figure 1. Possible scenarios of ionic phenomena in the LAO–STO system: (a) surface ion injection, (b) interface ion injection, and (c) bulk ion injection. The ionic carriers are shown by solid circles, and electronic carriers (holes) are shown by dotted circles. In case (a), the ions deposited on surface are compensated by the electronic carriers accumulated at the interface. The potential energy of the ion is infinite in the bulk. In case (b), the potential energy for the ions has deep minima at the surface (S) and interface (I), and ions can be injected to the interface (ionic shuttle between surface and interface). Compensation by the electronic carriers forms a conductive channel. In case (c), the potential energy profile for ions is more shallow and ions can be injected in the bulk of LAO and STO phases (or one of these), with small preference for segregation at the interface. In thermodynamic equilibrium, ion and electron concentration profiles are determined by the potential energy surface and configurational entropy.

formation of 2DEG in LAO–STO. Notably, these surface electrochemical mechanisms are relevant to other functional oxide surfaces, including ferroelectrics.[35,36]

On the basis of existing theoretical analyses, both the LAO surface and LAO–STO interface can be preferential sites for vacancy segregation. The natural question arising in this context is the localization of the oxygen vacancies (and generally mobile ionic species) introduced during film growth and the charge-writing process (Figure 1). While the ion deposition on oxide surfaces is well-recognized, we note that injection of vacancies in the bulk under conditions of high bias stress is possible even at room temperature. Indeed, both LAO and STO are (upon proper doping) well-recognized ionic conductors.[37] While classical oxygen-exchange studies driven by chemical potential gradients are generally limited to 500–700 °C,[38,39] application of high electric fields facilitates migration (*i.e.*, field driven) transport of ionic species even at low temperatures.[40,41] For bulk oxides, these phenomena were long explored in the context of ferroelectric fatigue.[42,43] Recently, extensive studies of these phenomena were reported in the context of resistive switching in transition metal oxides such as STO[44] and $BiFeO_3$.[45,46] However, the nanoscale nature of the LAO–STO system significantly limits application of classical electrochemical techniques.

Here, we explore the reversible and irreversible electrochemical phenomena on the LAO–STO surface in ambient conditions using a recently introduced method of electrochemical strain microscopy (ESM), developed for Li-ion[47,48] and oxygen conductor materials.[49]

RESULTS AND DISCUSSION

Time-Dependent Electrochemical Strain Spectroscopy of LAO–STO. The ESM is based on the detection of the reversible bias-induced strains mediated by ionic motion. The sharp (10–30 nm) scanning probe microscopy (SPM) tip concentrates an electric field in a nanoscale volume of material, resulting in the injection/annihilation of oxygen vacancies and subsequent vacancy transport and migration induced by the bias. The vacancy movement results in localized strain under the tip detected through dynamic surface displacement. This strain detection approach enables probing volumes 10^6–10^8 times smaller than accessible through Faradaic current-based electrochemical methods.[50,51] For materials such as cubic yttria-stabilized zirconia (YSZ),[49] the bias-induced displacement can be purely ascribed to ionic motion, while in materials such as $SrTiO_3$, the additional contributions to the signal stem from deformation potential effects and latent ferroelectric instability.[52,53] While in certain cases the physical and ionic mechanisms can be separated through the time dependence of the response,[54,55] in general, the origins of electromechanical coupling can only be understood in the context of known materials properties. Note that the experimental approach in ESM is equivalent to that of piezoresponse force microscopy (PFM), with the primary difference being their signal formation mechanisms (ionic motion *versus* piezoelectric coupling).

The preliminary studies of the LAO–STO system have shown that application of electric bias ("poling") induces strong electromechanical response that cannot be ascribed to electrostatic interactions, in agreement with previous studies by the Gruverman and Eom groups.[56] In that work, the authors illustrated the (a) presence of electromechanical response on the LAO–STO surface and (b) hysteresis loops both for bare and electrode-covered surfaces, reminiscent of that for ferroelectric materials. The bias pulse-induced response was observed to decay with time, with the relaxation rate strongly dependent on bias pulse magnitude and duration. This behavior and slow relaxation of the signal (under conditions excluding electrostatic tip–surface interactions) hints at several possible electrochemical mechanisms, such as direct vacancy injection into the material (Figure 1b,c), surface-charge stabilized (Figure 1a) ferroelectric states, or electrostrictive response. However, the role of time dynamics (*i.e.*, whether the hysteresis loops are thermodynamic or kinetic in nature) and role of irreversible electrochemical processes has not been established.

To explore these phenomena systematically, we performed dynamic electrochemical strain microscopy

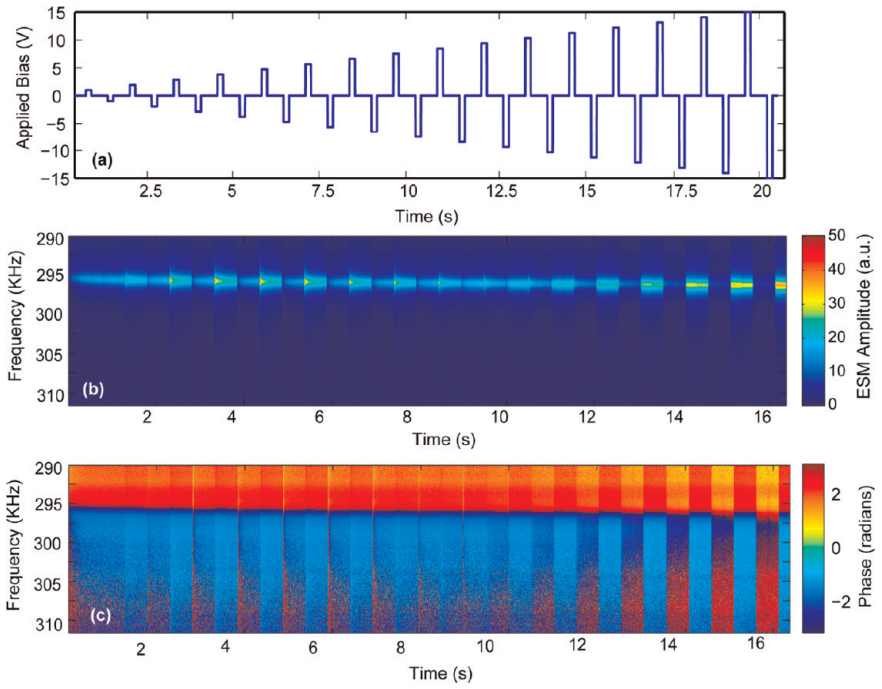

Figure 2. (a) Envelope of the bias waveform at a single spatial pixel in a D-ESM experiment composed by a series of bipolar impulses of increasing amplitude. After each on-pulse, the relaxation of electromechanical response is measured using a train of 128 BE waveforms (not shown). Two-dimensional (b) amplitude and (c) phase spectrograms depicting the evolution of cantilever response as a function of frequency (vertical axis) and time (horizontal axis). For simplicity, shown is the evolution of response only during the off-states, hence different time scales in (a) and (b,c). The response is averaged over 20 × 20 pixels with 50 nm grid spacing.

(D-ESM) measurements. In D-ESM, the tip is excited using a set of pulses (~50 ms) amplitude modulated by a linearly increasing waveform, as shown in Figure 2a. The differential detection in band excitation (BE) mode[57] is employed to detect the dynamic (~300 kHz) electrochemical strains. The BE method allows us to compensate for position-dependent tip−surface resonance frequencies (indirect topographic cross-talk[58]) and determine the bias-induced changes on the mechanical properties of material.[59] Here, a train of BE waveforms is applied after each dc bias pulse to detect the time relaxation of the signal. A 2D ESM spectrogram representing the response modulus as a function of frequency and time obtained after each bias pulse is shown in Figure 2b. These 2D data describe the frequency- and voltage-dependent response of material at each location to bias pulses of increasing amplitude.

To extract local spectroscopic responses, the BE spectrum at each location is analyzed using simple harmonic oscillator (SHO) deconvolution[57] to yield the response amplitude, A, resonant frequency, ω_r, and Q-factor, Q, of the cantilever. The response amplitude is the measure of electrochemical (or piezoelectric) activity of material; the resonance frequency is controlled by the mechanical properties and size of tip−surface junction, and Q-factor is a measure of the total (mechanical and electromechanical) losses in the system. This analysis allows for the decoupling of the voltage-dependent evolution in electromechanical, mechanical, and dissipative (*e.g.*, loss modulus) properties of the material, thus obviating topographic cross-talk effects.

Here, the measurements were performed over 20 × 20 spatial grid of locations (50 nm pixel to pixel spacing) to provide sufficient statistics. The principal component analysis[60−63] of the full time-dependent D-ESM data suggests that spatial variability of signal is relatively small (evidencing high uniformity of the film), and hence the D-ESM signal averaged over the grid offers representative behavior. The averaged response curve over spatial location is shown in Figure 3a, illustrating the evolution of ESM response (defined as mixed signal, $RE = A\cos(\varphi)$, where A is response amplitude and φ is phase) following the application of progressively higher amplitude bias pulses. Note the highly complex relaxation behavior as a function of pulse magnitude.

To simplify the data analysis, the response is replotted in Figure 3b−d as amplitude, resonant frequency, and Q-factor only during the bias off-states. Several characteristic regions of dissimilar voltage behavior are clearly seen. For low biases (V_{pulse} < ~3.5 V), no relaxation is visible and the signal is almost bias-independent. Strong initial changes in Q and ω_r can be ascribed to either the fitting error for small signal amplitudes or initial formation of tip−surface contact. For higher biases (3.5 V ≪ V_{pulse} ≪ 10 V), the bias pulse induces strong change in electromechanical

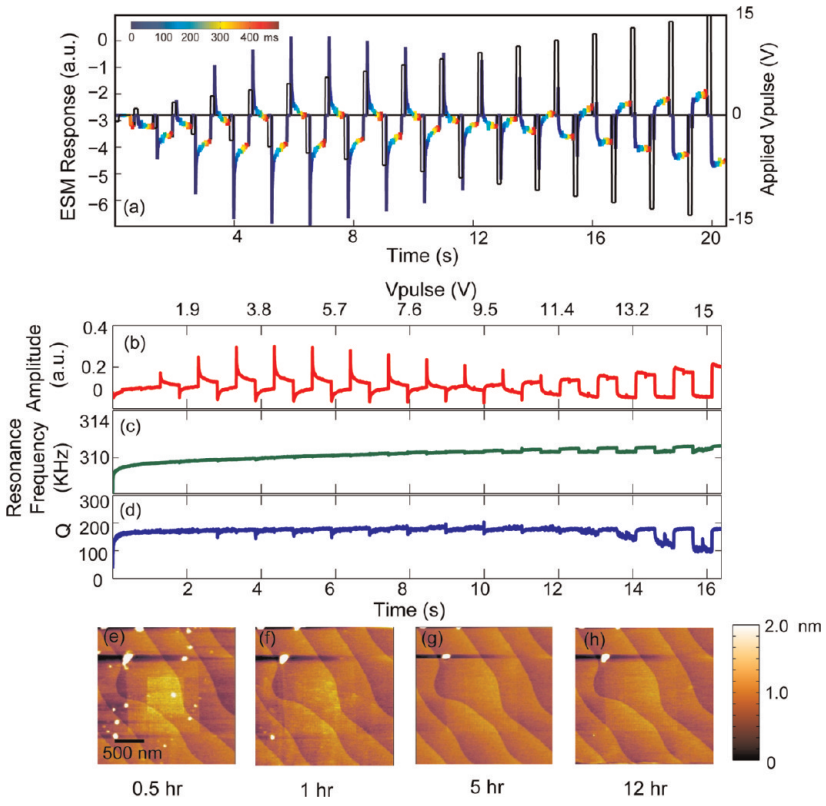

Figure 3. (a) Evolution of the response amplitude during the full D-ESM measurements. Signal relaxation is probed only during the off-state. Color coding is used to indicate the time after pulse. The evolution of (b) amplitude, (c) resonance frequency, and (d) *Q*-factor of the cantilever during the off-segments. Shown is the response averaged over 20 × 20 spatial locations with 50 nm grid spacing. (e) Surface topography of the LAO−STO surface immediately after D-ESM measurements and its relaxation after (f) 1 h, (g) 5 h, and (h) 12 h. Note the clearly visible surface deformation of ~0.5 nm (comparable to step edge height) that slowly relaxes to 0.2 nm after 12 h.

response with subsequent rapid relaxation. Interestingly, the effective relaxation time rapidly decreases with V_{pulse}. The relaxation is almost complete (no remanent response) within the measurement interval. This process is associated with only very weak changes in resonant frequency (less than 2 kHz for negative polarity) after negative pulses and is almost invisible compared to the general background line. The *Q*-factors show small drops following negative pulses. Changes in ω_r and *Q* relax rapidly with time; that is, they are transient on the time scale of several seconds.

Finally, for high voltages (V_{pulse} > ~10 V), the relaxation process becomes almost undetectable within the measurement level employed. Note that this is due to the *decrease* of relaxation time; that is, relaxation becomes faster than minimal time accessible in D-ESM experiment (4 ms). At the same time, the nonrelaxing (on the time scale of spectroscopic experiment, ~20 s) component appears, so that overall time dependence of the electromechanical response resembles that of ferroelectric material; that is, a series of time-independent multilevel bias-induced states are observed (that in the voltage domain will manifest as classical hysteresis loop). Notably, at these biases, a strong change in resonant frequency (higher for positive pulses) is observed. Similar to response amplitude, the resonant frequency is almost independent of time after bias application, and frequency shift between positive and negative pulses increases with V_{pulse}. For the highest biases, changes in *Q*-factor are also observed.

The relaxation behavior is quantified using the phenomenological fitting function method. In this, each segment of the relaxation curve is fit using the exponential function

$$RE(V,t) = A_0(V) + A_1(V)\exp\left(-\frac{t}{\tau(V)}\right) \qquad (1)$$

where $RE(V,t)$ is response measured at delay time, t, after the application of the pulse of magnitude, V. The nonrelaxing signal (offset) is $A_0(V)$, relaxation amplitude is $A_1(V)$, and relaxation time is $\tau(V)$. The fit by eq 1 is performed on the response averaged over multiple locations (x, y); that is, a single data set $\langle RE(V,t)\rangle_{x,y}$ is fit. The corresponding parameters are shown in Figure 4a. Alternatively, the fit is performed over D-ESM spectra from dissimilar locations, and averaged fitting parameters $A_0^{av} = \langle A_0(V)\rangle_{x,y}$, $A_1^{av} = \langle A_1(V)\rangle_{x,y}$, and $\tau^{av} = \langle \tau(V)\rangle_{x,y}$ are plotted in Figure 4b. Note that the deviation between the fit of the average and average of the fit data sets is relatively small, indicative of an adequate relaxation model.

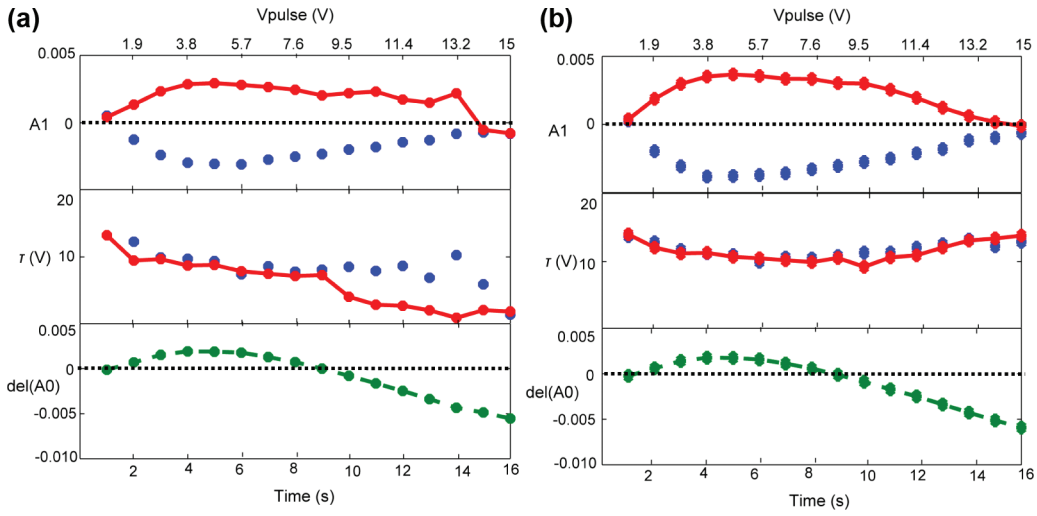

Figure 4. Bias dependence of exponential fit parameters for (a) spatially averaged and (b) single-point D-ESM data.

The data illustrates the aspects of relaxation behavior as seen in Figure 3. The relaxation amplitude is increasing for V_{pulse} < 3−3.5 V and then slowly decreases, becoming zero at ∼15 V. The relaxation amplitudes are almost equal for positive and negative bias pulses. The relaxation times become smaller with V_{pulse}. Finally, the offset (nonrelaxing signal) becomes significant above 10 V.

Note that, in general, the relaxation kinetics do not necessarily follow the functional form of eq 1. However, in the absence of knowledge of physics-based mechanisms (*i.e.*, *a priori* known functional form of relaxation), the intrinsically high noise level of the D-ESM experiment precludes more definitive model selection for single point data. At the same time, spatially averaged data have a lower noise level, but small variability of material responses between dissimilar locations can change the relaxation function (*e.g.*, average of multiple exponentials with uniformly distributed relaxation times yields a logarithmic or stretched exponential law). This limitation can be partially circumvented through the use of multivariate statistical methods; however, given the lack of defined physical models, we defer detailed quantitative analysis to future studies.

Overall, the bipolar D-ESM data shown in Figures 3 and 4 suggest the presence of at least two different electrochemical processes. The first process is activated at relatively low biases, V_{pulse} > 3.5 V, and the corresponding relaxation time decreases rapidly with pulse bias. Only weak transient changes in resonant frequency and *Q*-factor are observed; that is, the mechnical properties of tip−suface contact are not affected. The second process is activated at higher biases, V_{pulse} > ∼10 V. This process is nonrelaxational (or characteristic relaxation times are well above the experimentally probed segment, 4 ms) and is associated with significant changes in resonant frequency. This behavior is highly unusual and has not been previously observed in D-ESM studies of other ionic or mixed electronic−ionic conductive oxides (yttria-stabilized zirconia, samaria-doped ceria, lanthanum−strontium cobaltite), for which voltage-independent (within resolution) relaxation behavior is observed.

Following the D-ESM data acquisition, we note that the bias application resulted in formation of small (300−500 pm) surface deformations. While below or comparable to unit step height (0.4 nm), these displacements are clearly seen on the topographic image. These static deformations slowly decrease with time, almost completely relaxing after ∼12 h. We note that formation of such static deformation is a strong argument toward the electrochemical processes including strongly bound surface species or in the bulk of material. The formation of water droplets in the tip−surface junction or adsorption of weakly bound surface adsorbates would lead neither to significant changes in surface topography nor shifts in resonant frequency.

Unipolar D-ESM Measurements: Separating Cathodic and Anodic Processes. To gain further insight into mechanisms of local bias-induced phenomena on the LAO−STO surface, we attempt to separate the cathodic and anodic processes using unipolar waveforms. In these measurements, the waveform sent to the tip is similar to that in Figure 2a but contains only positive (or negative) pulses. The same bias range (up to V_{pulse} = 15 V) is explored in bipolar, positive, and negative unipolar experiments.

The results of the unipolar D-ESM experiments are shown in Figure 5. In the voltage interval V_{pulse} < ∼8 V (*i.e.*, for significantly higher biases then strong relaxation in bipolar D-ESM), virtually no relaxation is observed in the unipolar waveforms. However, the changes in corresponding base lines are relatively weak. At the same time, in the region of V_{pulse} > ∼8 V (*i.e.*, no relaxation in bipolar measurements), the strong

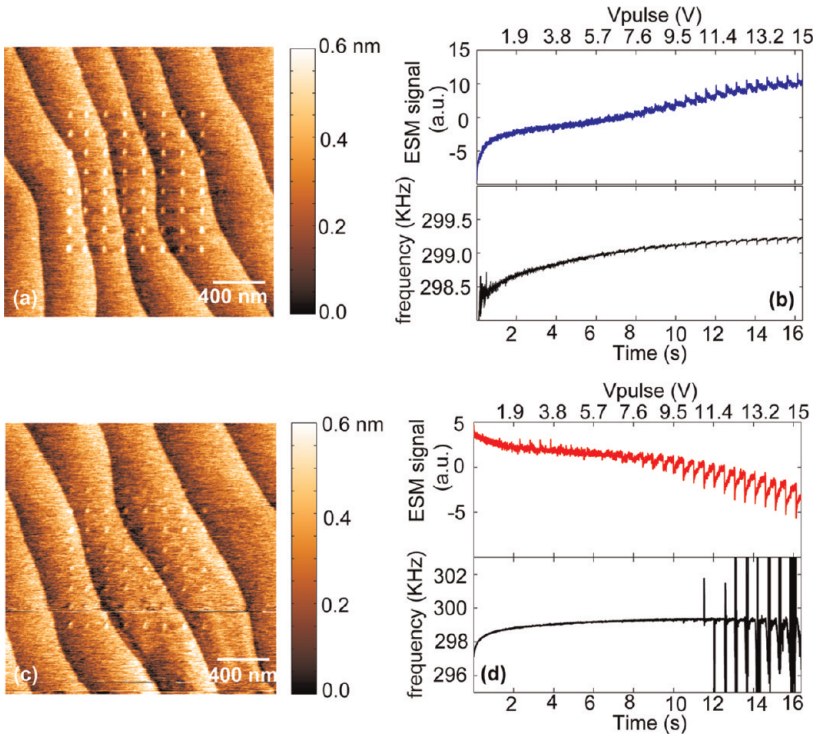

Figure 5. Positive (a,b) and negative (c,d) unipolar D-ESM data on the LAO–STO surface. (a,c) Surface topography after measurements and (b,d) relaxation of ESM signal.

relaxation and significant baseline shifts are observed for both positive and negative unipolar data. On the basis of the examination of curves in Figure 5b,d, we observe the following features of positive and negative unipolar ESM: (1) relaxation for negative biases starts slightly earlier (albeit within the error of experiment); (2) relaxation amplitude is markedly higher for negative biases; (3) relaxation times are almost bias-independent for both positive and negative waveforms; (4) both waveforms result in formation of static surface deformations; however, these are much more pronounced for positive biases (final height of 0.5 nm as compared to 0.3 nm for negative).

Static Deformations on the LAO–STO Surface. The characteristic aspect of bipolar, positive, and negative bias pulse application on the LAO–STO surface is the formation of surface deformations. These can be observed as spatially uniform "swelling" of material for dense grids, as shown in Figure 3e–h, or formation of individual "particles" for sparse grids, as shown in Figure 5a,c. The typical magnitude of the static deformations is relatively small, on the scale of 300–500 pm for bias of 10 V, and is below or comparable to the unit step height on the LAO surface. This smallness of surface deformation and their visibility only above typical writing voltages for LAO–STO may explain why this phenomenon was not previously reported.

Here, we explore bias dependence particle formation and the interplay between particle and hysteretic loop formation systematically. For these measurements, the bipolar sequence of bias pulses of prescribed amplitudes are applied over a square spatial grid of points. The pulse magnitude is constant along one direction (fast scan axis) and is ramped linearly along the other direction (slow scan). Surface topography is measured both before and after the bias application. In such a way, the bias-dependent tip-induced irreversible electrochemical processes can be ascertained with a high degree of statistical significance. Furthermore, this approach establishes the role of mobile surface species in the particle formation process, as discussed below.

The results of the unipolar experiment are shown in Figure 6. The particle formation is observed only for biases $V_{pulse} > 8$ V. The comparison of the data in Figure 2 and Figure 6 illustrates that particle formation is a hallmark of a high-voltage (slow) electrochemical process on the LAO–STO surface. Furthermore, particle formation is thus consistent with the resonance frequency shifts and changes in *Q*-factor observed in this bias range.

A number of conclusions can be derived from the particle morphology. Figure 6b,c illustrates that particles have a characteristic "doughnut" shape. We attribute this to the fact that particles initially form in the region adjacent to the tip–surface junction but not directly below the tip. The hole in the center thus corresponds to the original tip location.

Finally, after the application of high bias pulses, the particle sometimes can be shifted by lateral tip motion, as shown in Figure 6c. In several cases when this particle dislocation by the tip was observed, the region

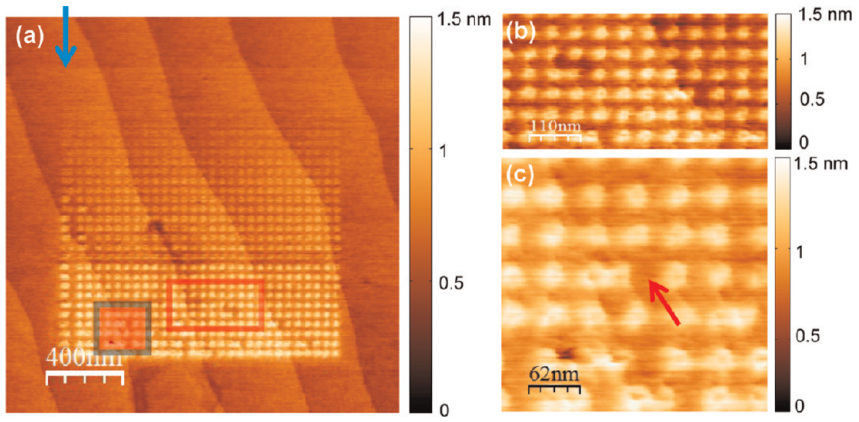

Figure 6. Bias-dependent particle formation on the LAO–STO surface. (a) Surface topography after bias pulse application (30 × 30 grid, voltage amplitude from 1 to 30 V). (b) Zoom-in of (a). (c) Zoom-in on the region with moved particle (marked by arrow).

of the surface underneath the particle does not show a clearly visible (*i.e.*, deeper then 30–100 pm) depression. This observation strongly suggests that particle formation and relaxation, while kinetically very slow (>10 h), do not involve the irreversible removal of material from the surface and rather involve only surface species. Similar behaviors are observed for negative pulses.

Previously, the presence of electromechanical response and hysteresis in LAO–STO was reported.[56] To explore the relationship between hysteresis loop formation, relaxation, and particle formation, we have performed the simultaneous hysteresis loop measurements with increasing bias amplitude, similar to the grid experiments in Figure 6. Shown in Figure 7a,b is surface topography before and after the hysteresis loop measurements. The loop area *versus* bias is shown in Figure 7d, illustrating that the loop opening is observed at biases of ~7 V, well below particle formation threshold.

To quantify the bias-induced particle formation, the images were spatially aligned using the step edges as reference points. The particle size and height were determined from the differential image between the initial topography image and the image obtained after bias application, as shown in Figure 7c, and the dependence of these parameters on the applied bias window is shown in Figure 7e. Note that, in this case, particle formation is observed at biases >12 V. Furthermore, both volume and height of the particles change similarly. This observation can be interpreted as purely vertical growth of the particle; however, given the tip convolution effect on the lateral object size in SPM, this conclusion is not unambiguous.

Finally, we note that in the expeirments where hysteresis loops were measured, the particle size is non-uniform within the grid and becomes larger to the edges of the scanned area (in comparison, in single pulse experiments such as Figure 6, the particle size is uniform within the grid). This observation suggests that the particle formation process is limited by the diffusion of surface mobile species available in (relatively) small amounts. At the same time, hysteresis loop opening is spatially uniform within the image, suggesting that there are different origins of (irreversible) particle formation process and (reversible) hysteresis loop opening.

Electrostatic Hysteresis Measurements. To complement the ESM measurements and gain further insight into the dynamics of charge behavior in the system, we have performed Kelvin probe force microscopy (KPFM) studies. While ESM is sensitive to electromechanical response and is only weakly affected by electrostatic forces, KPFM provides complementary information on the changes in work function and presence of uncompensated surface charges but is insensitive to small surface deformations.

Here, tip-induced surface potential is measured following the poling of the surface as a function of poling bias, as shown in Figure 8. These studies were performed on the surface which was uniformly prepoled at ±20 V, providing an averaged KPFM hysteresis loop, as shown in Figure 8a. Note while there is a measurable hysteresis, the shape of the loop and its position are very different from the ESM loops. Furthermore, the KPFM hysteresis indicates the presence of hysteretic charging but cannot differentiate surface and bulk charge injection.

Electrochemical Processes in the LAO–STO System. The observations of the electromechanical response, hysteresis loops, bias-dependent relaxation, and spatial variability of particle formation and hysteresis loop opening on the LAO–STO surface indicate the presence of at least two disparate electrochemical processes. Below, we attempt to analyze the possible origins of observed behaviors and their implication for LAO–STO physics.

The observations of the high-frequency electromechanical response on the LAO–STO surface, in agreement with an earlier report (ref 56), are surprising *per se*.

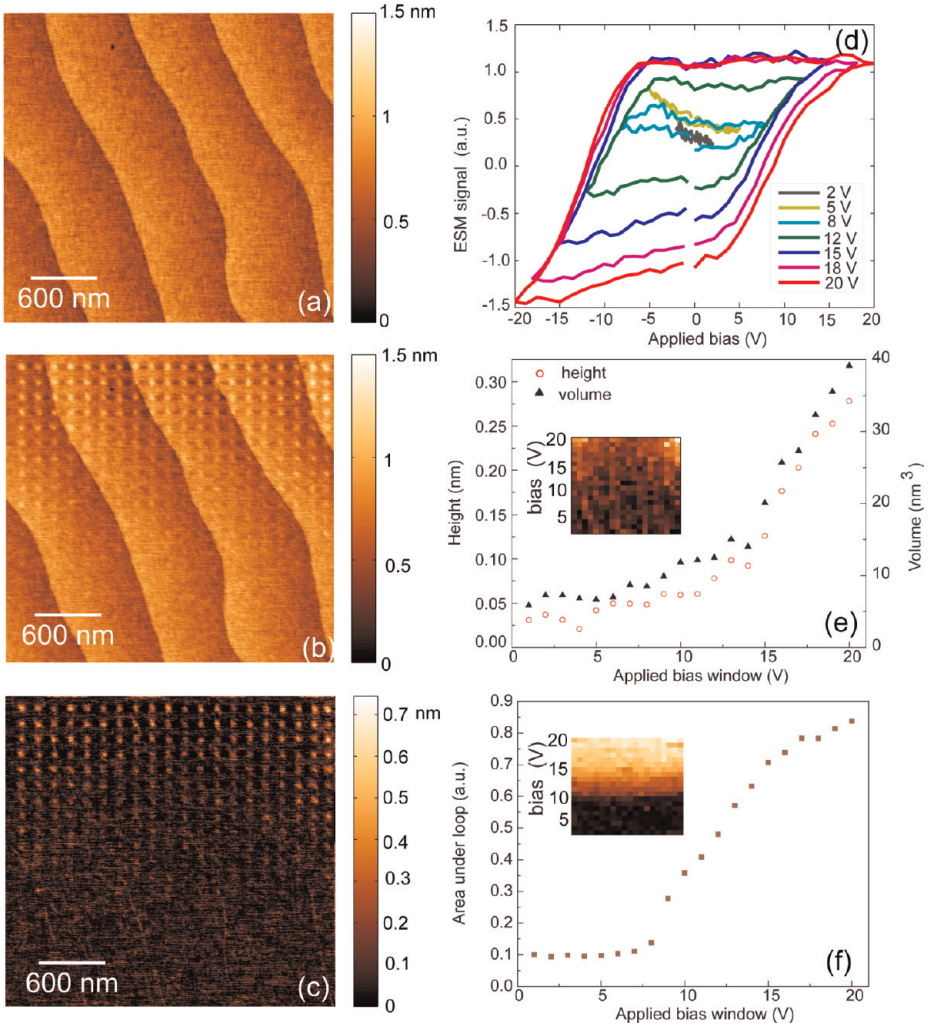

Figure 7. Correlation between particle and hysteresis loop formation. Surface topography (a) before and (b) after the application of bias pulse sequence. (c) Differential topographic image from which particle parameters are determined. (d) Bias dependence of hysteresis loops. Bias dependence of (e) particle height and volume and (f) hysteresis loop opening.

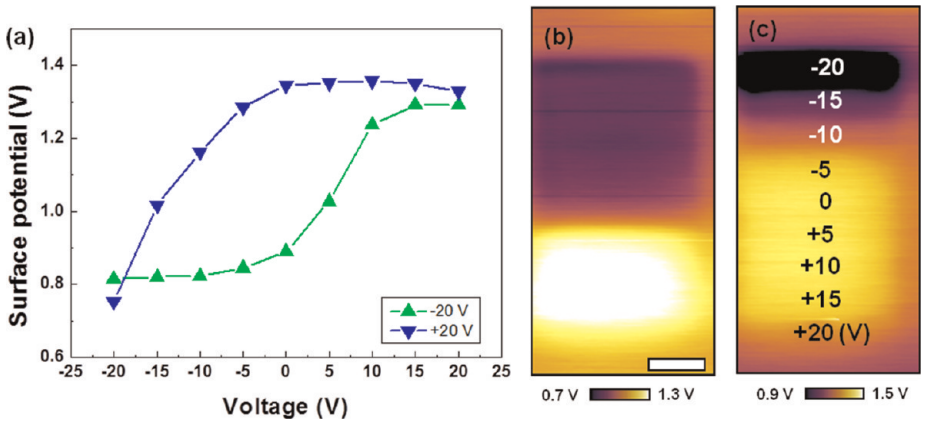

Figure 8. (a) Tip-induced surface potential as a function of poling bias on the surface uniformly prepoled by ±20 V. Each tip bias surface potential is averaed from each rectangular pattern. (b,c) Surface potential images of the area scanned with the applied biases from −20 to +20 V to the conductive probe for prepoled surface by (b) −20 V and (c) +20 V. The scale bar shown in (b) is 1 μm.

Note that both LAO and STO are centrosymmetric materials and hence, by definition, are not piezoelectric. However, LAO interfaces have a nonzero polarization.[64] For a nanometer-sized thin film, as the case here, the surface-bound polarization charge may not be perfectly screened (ionically or electronically), leaving a built-in

internal electric field in the film.[34,65] This built-in field induces a dielectric response (and a corresponding electrostrictive effect[66]) and, importantly, destroys the inversion symmetry allowing for a piezoelectric signal.

Alternatively, the electromechanical response that constitutes the ESM or PFM signal can be ascribed to either surface or bulk ionic dynamics (similar to recent studies on YSZ[49]) or hysteretic surface charging coupled with the electrostriction effects or field-induced ferroelectric phase stability. Note that for thin films, the boundary between purely physical (*e.g.*, ferroelectric polarization) and electrochemical phenomena is not sharp, for example, as analyzed by Highland and Stephenson.[67,68] In LAO, surface ionic formation is likely to be coupled to its nonzero polarization.[56] Specifically, surface redox processes (*e.g.*, the creation of oxygen vacancies) have been shown to be thermodynamically stable at the LAO surface.[34] The equilibrium density of these surface oxygen vacancies depends on the potential drop across the film and hence poling voltage. This bias-induced modulation of the density of surface oxygen vacancies would produce a localized electrochemical strain response, as measured by ESM. The presence of the surface or bulk charge injection and injection hysteresis are directly confirmed by the KPFM hysteresis loops.

In ambient environment, surface bias-induced phenomena additionally include electrocapillary water condenstaion at the tip−surface junction, splitting of water molecules, and/or migration of surface ionic species (most dominantly protons, H^+, and hydroxyl, OH^-). Both types of ions can bind to the metal oxide surfaces. The process can also be affected by presence of CO_2 and hydrocarbons. For unity sticking probability, the adsorption rate can be estimated as $N/A = p/(2\pi mkT)^{1/2}$, where p is equilibrium pressure, A is area, N is evaporation rate, and m is mass. For ~1 atm, the filling time of a single monolayer is on the order of 2 μs. Hence, even a minute (~10 ppm) level of impurities can be adsorbed with approximately monolayer coverage on the time scale of the spectroscopic experiment. Furthermore, the strong electric fields in the tip−surface junction can give rise to unusual electrochemistry, as exemplified by formation of carbonaceous deposits from CO_2 in a tip−surface junction at several tens of volts.[69]

The bulk electrochemical processes within the oxide are equally varied and can include injection and annihilation of oxygen vacancies due to oxygen evolution/reduction reaction, injection of protons and hydroxides, and more disruptive electrochemical processes associated with the change of connectivity and composition of cationic sublattices. Finally, open is the issue of the combined water/electrochemical effects, such as electrochemistry in the monolayers of hydroxylated metal oxide species or surface vacancy populations that were reported recently for $SrTiO_3$,[70] $BaTiO_3$,[31,71] and $PbTiO_3$.[29,30,67]

In interpreting the observations for the LAO−STO system studied here, we note that the irreversible material degradation associated with cationic demixing or changes in the lattice connectivity (*e.g.*, formation of crystallographic shear structures) would result in permanent formation of protrusions of material surface and formation of depressed areas after removal. Furthermore, these processes are inconsistent with slow zero-field relaxation present in the LAO−STO system. Hence, we attribute the observed ESM response to surface electrochemical reactions (water splitting) possibly assisted by reversible oxygen vacancy dynamics in LAO/STO.

The fast relaxation process can be ascribed to extrinsic behaviors such as electrocapillary water condensation, charging of surface or surface water layer, or reversible injection of vacancies in the material. The fact that strong relaxation for low biases (below 8 V) is observed for bipolar but not unipolar pulses favors electrochemical mechanisms, including vacancy injection and water dissociation and migration on the surface. Given that driving force for electrocapillary condensation is quadratic in voltage, the relaxation due to the forming water meniscus in the tip−surface junction can be expected to be identical for unipolar and bipolar waveforms. The relaxation observed in unipolar measurements at higher biases (>8 V) can then be attributed to surface overcharging, that is, injection of protons and hydroxyles above the stoichiometry. Note that the clear delineation between reversible oxygen vacancy dynamics and surface water splitting can be achieved only under proper atmospheric control.

The slow high-voltage process can be associated with vacancy injection in LAO/STO or accumulation of high molecular weight (*e.g.*, hydrocarbons) species on the surface. The morphology of formed particles, specifically the characteristic doughnut-like shape and the fact that particles can be shifted without leaving an impression in the surface, suggests that the accumulation of low-mobility species (hydrocarbon contaminants and hydroxylated lanthanum and aluminum species) is the most likely explanation. In particular, the doughnut-like shape (*i.e.*, particle with the impression of the tip) suggests that the material was accumulated in the tip−surface junction after the contact was established and/or that material has relatively low (0.1−1 GPa) Young's modulus, well below that expected for perovskites (~100 GPa). This assumption is further reinforced by the spatial nonuniformity of particle sizes, with preferential growth at the edge of the scanned area. On the basis of this analysis, the slow electrochemical process seems to be attributable to the field-controleld surface contaminant dynamics.

SUMMARY

To summarize, tip-induced electrochemical phenomena on the LAO–STO surface are explored using unipolar and bipolar dynamic electrochemical strain microscopy measurements. The D-ESM demonstrates the presence of at least two processes well-separated in bias, suggesting that charge-writing behavior in this system includes a strong electrochemical component and is more complicated than simple screening by surface adsorbates. The analysis of response relaxation, frequency shifts, and static surface deformations suggests that a reversible low-voltage process can be attributed to either surface charging due to electrochemical water layer splitting or reversible oxygen vacancy formation on or close to the material surface. The slow (irreversible) high bias process associated with surface deformation can be attibuted to the accumulation of hydrocarbon or hydroxylated La and Al containing species in the tip–surface junction but is unlikely to be associated with irreversible vacancy injection in the material or changes in connectivity or composition in cation sublattices. Future studies in controlled environments and combined chemical imaging studies can reveal the exact nature of the forming particulates.

Overall, D-ESM offers a powerful tool to probe local bias-induced reversible and irreversible electrochemical reactions on complex surfaces. While the LAO–STO explored here exibits remarkable spatial uniformity of electrochemical responses, a similar approach can be used for spatially inhomogeneous systems. Finally, the combinations with other local techniques, such as micro-Raman or NSOM, variable atmosphere measurements, and *ex situ* local analysis of reaction regions, can establish the exact chemical origins of the observed phenomena.

MATERIALS AND METHODS

The samples studied in this paper are 3 u.c. LAO films grown on Ti-terminated STO(001) substrates. The LAO layer were grown by the pulsed-laser deposition (PLD) system equipped with high-pressure reflection high-energy electron diffraction (RHEED), which enabled the layer-by-layer growth of the thin films to be monitored *in situ* during growth. Before deposition, STO substrates were etched using buffered HF acid for 60 s to maintain Ti termination before LAO deposition. The STO substrates were annealed in oxygen at 1000 °C for 6 h to create atomically smooth surfaces with a unit cell step after chemical etching. To grow heterostructures, substrates were attached to a resistive heater and positioned 5.8 cm from the target. A KrF excimer laser (248 nm) beam was focused on a stoichiometric LAO single crystal target to an energy density of 1.5 J/cm^2 and pulsed at 3 Hz. LAO layers were grown at substrate temperatures at 550 °C and oxygen pressures of 10^{-3} mbar and cooled to room temperature. During growth, LAO layers exhibited clear RHEED intensity oscillations which indicate a layer-by-layer mode.

Atomic force microscopy (AFM) and ESM measurements were performed with a commercial system (Asylum Research Cypher) additionally equipped with LabView/MatLab-based band excitation controller implemented on a NI-5122/5412 fast AWG and DAQ cards. ESM imaging and spectroscopy was performed with 200–400 kHz 2V_{pp} band excitation signal applied to a metal coated tip. The spectroscopic measurements were performed at ~1 s/pixel waveform with 2 ms at each dc voltage step. Mapping of the electromechanical response was done typically on a 50 × 50 points grid with a spacing of 20 nm, albeit other spacing and image sizes were also used. All measurements were performed with the biased tip in direct contact with the LAO–STO surface in ambient air and without any additional protective coating.

Conflict of Interest: The authors declare no competing financial interest.

Acknowledgment. Research was supported (A.K., S.V.K.) by the U.S. Department of Energy, Basic Energy Sciences, Materials Sciences and Engineering Division and performed at the Center for Nanophase Materials Sciences (S.J.), a DOE-BES user facility. The work at University of Wisconsin was supported by the National Science Foundation (NSF) under Grant No. DMR-0906443. N.C.B. and E.A. acknowledge the support by EPSRC.

REFERENCES AND NOTES

1. Ohtomo, A.; Hwang, H. Y. A High-Mobility Electron Gas at the $LaAlO_3/SrTiO_3$ Heterointerface. *Nature* **2004**, *427*, 423–426.
2. Thiel, S.; Hammerl, G.; Schmehl, A.; Schneider, C. W.; Mannhart, J. Tunable Quasi-Two-Dimensional Electron Gases in Oxide Heterostructures. *Science* **2006**, *313*, 1942–1945.
3. Caviglia, A. D.; Gariglio, S.; Reyren, N.; Jaccard, D.; Schneider, T.; Gabay, M.; Thiel, S.; Hammerl, G.; Mannhart, J.; Triscone, J. M. Electric Field Control of the $LaAlO_3/SrTiO_3$ Interface Ground State. *Nature* **2008**, *456*, 624–627.
4. Li, L.; Richter, C.; Paetel, S.; Kopp, T.; Mannhart, J.; Ashoori, R. C. Very Large Capacitance Enhancement in a Two-Dimensional Electron System. *Science* **2011**, *332*, 825–828.
5. Reyren, N.; Thiel, S.; Caviglia, A. D.; Kourkoutis, L. F.; Hammerl, G.; Richter, C.; Schneider, C. W.; Kopp, T.; Ruetschi, A. S.; Jaccard, D.; *et al.* Superconducting Interfaces between Insulating Oxides. *Science* **2007**, *317*, 1196–1199.
6. Dikin, D. A.; Mehta, M.; Bark, C. W.; Folkman, C. M.; Eom, C. B.; Chandrasekhar, V. Coexistence of Superconductivity and Ferromagnetism in Two Dimensions. *Phys. Rev. Lett.* **2011**, *107*, 056802.
7. Bert, J. A.; Kalisky, B.; Bell, C.; Kim, M.; Hikita, Y.; Hwang, H. Y.; Moler, K. A. Direct Imaging of the Coexistence of Ferromagnetism and Superconductivity at the $LaAlO_3/SrTiO_3$ Interface. *Nat. Phys.* **2011**, *7*, 767–771.
8. Cen, C.; Thiel, S.; Hammerl, G.; Schneider, C. W.; Andersen, K. E.; Hellberg, C. S.; Mannhart, J.; Levy, J. Nanoscale Control of an Interfacial Metal-Insulator Transition at Room Temperature. *Nat. Mater.* **2008**, *7*, 298–302.
9. Nakagawa, N.; Hwang, H. Y.; Muller, D. A. Why Some Interfaces Cannot Be Sharp. *Nat. Mater.* **2006**, *5*, 204–209.
10. Pentcheva, R.; Pickett, W. E. Avoiding the Polarization Catastrophe in $LaAlO_3$ Overlayers on $SrTiO_3$ (001) through Polar Distortion. *Phys. Rev. Lett.* **2009**, *102*, 017602.
11. Li, Y.; Yu, J. Polarization Screening and Induced Carrier Density at the Interface of $LaAlO_3$ Overlayer on $SrTiO_3$ (001). *J. Appl. Phys.* **2010**, *108*, 013701.
12. Hamann, D. R.; Muller, D. A.; Hwang, H. Y. Lattice-Polarization Effects on Electron-Gas Charge Densities in Ionic Superlattices. *Phys. Rev. B* **2006**, *73*, 195403.
13. Popovic, Z. S.; Satpathy, S.; Martin, R. M. Origin of the Two-Dimensional Electron Gas Carrier Density at the $LaAlO_3$ on $SrTiO_3$ Interface. *Phys. Rev. Lett.* **2008**, *101*, 256801.
14. Millis, A. J.; Schlom, D. G. Electron–Hole Liquids in Transition-Metal Oxide Heterostructures. *Phys. Rev. B* **2010**, *82*, 073101.

15. Willmott, P. R.; Pauli, S. A.; Herger, R.; Schleputz, C. M.; Martoccia, D.; Patterson, B. D.; Delley, B.; Clarke, R.; Kumah, D.; Cionca, C.; Yacoby, Y. Structural Basis for the Conducting Interface between $LaAlO_3$ and $SrTiO_3$. *Phys. Rev. Lett.* **2007**, *99*, 155502.
16. Qiao, L.; Droubay, T. C.; Shutthanandan, V.; Zhu, Z.; Sushko, P. V.; Chambers, S. A. Thermodynamic Instability at the Stoichiometric $LaAlO_3/SrTiO_3$ (001) Interface. *J Phys.: Condens. Matter* **2010**, *22*, 312201.
17. Zhong, Z. C.; Xu, P. X.; Kelly, P. J. Polarity-Induced Oxygen Vacancies at $LaAlO_3/SrTiO_3$ Interfaces. *Phys. Rev. B* **2010**, *82*, 165127.
18. Zhang, L. X.; Zhou, X. F.; Wang, H. T.; Xu, J. J.; Li, J. B.; Wang, E. G.; Wei, S. H. Origin of Insulating Behavior of the p-Type $LaAlO_3/SrTiO_3$ Interface: Polarization-Induced Asymmetric Distribution of Oxygen Vacancies. *Phys. Rev. B* **2010**, *82*, 125412.
19. Herranz, G.; Basletic, M.; Bibes, M.; Carretero, C.; Tafra, E.; Jacquet, E.; Bouzehouane, K.; Deranlot, C.; Hamzic, A.; Broto; *et al.* High Mobility in $LaAlO_3/SrTiO_3$ Heterostructures: Origin, Dimensionality, and Perspectives. *Phys. Rev. Lett.* **2007**, *98*, 216803.
20. Siemons, W.; Koster, G.; Yamamoto, H.; Harrison, W. A.; Lucovsky, G.; Geballe, T. H.; Blank, D. H. A.; Beasley, M. R. Origin of Charge Density at $LaAlO_3$ on $SrTiO_3$ Heterointerfaces: Possibility of Intrinsic Doping. *Phys. Rev. Lett.* **2007**, *98*, 196802.
21. Kalabukhov, A.; Gunnarsson, R.; Borjesson, J.; Olsson, E.; Claeson, T.; Winkler, D. Effect of Oxygen Vacancies in the $SrTiO_3$ Substrate on the Electrical Properties of the $LaAlO_3/SrTiO_3$ Interface. *Phys. Rev. B* **2007**, *75*, 121404.
22. Chambers, S. A.; Engelhard, M. H.; Shutthanandan, V.; Zhu, Z.; Droubay, T. C.; Qiao, L.; Sushko, P. V.; Feng, T.; Lee, H. D.; Gustafsson, T.; *et al.* Instability, Intermixing and Electronic Structure at the Epitaxial $LaAlO_3/SrTiO_3$ (001) Heterojunction. *Surf. Sci. Rep.* **2010**, *65*, 317–352.
23. Xie, Y. W.; Bell, C.; Hikita, Y.; Hwang, H. Y. Tuning the Electron Gas at an Oxide Heterointerface *via* Free Surface Charges. *Adv. Mater.* **2011**, *23*, 1744–1747.
24. Xie, Y. W.; Bell, C.; Yajima, T.; Hikita, Y.; Hwang, H. Y. Charge Writing at the $LaAlO_3$ /$SrTiO_3$ Surface. *Nano Lett.* **2010**, *10*, 2588–2591.
25. Bi, F.; Bogorin, D. F.; Cen, C.; Bark, C. W.; Park, J. W.; Eom, C. B.; Levy, J. "Water-Cycle" Mechanism for Writing and Erasing Nanostructures at the $LaAlO_3/SrTiO_3$ Interface. *Appl. Phys. Lett.* **2010**, *97*, 173110.
26. Kalinin, S. V.; Bonnell, D. A. Screening Phenomena on Oxide Surfaces and Its Implications for Local Electrostatic and Transport Measurements. *Nano Lett.* **2004**, *4*, 555–560.
27. Kalinin, S. V.; Bonnell, D. A. Effect of Phase Transition on the Surface Potential of the $BaTiO_3$ (100) Surface by Variable Temperature Scanning Surface Potential Microscopy. *J. Appl. Phys.* **2000**, *87*, 3950–3957.
28. Cunningham, S.; Larkin, I. A.; Davis, J. H. Noncontact Scanning Probe Microscope Potentiometry of Surface Charge Patches: Origin and Interpretation of Time-Dependent Signals. *Appl. Phys. Lett.* **1998**, *73*, 123–125.
29. Fong, D. D.; Kolpak, A. M.; Eastman, J. A.; Streiffer, S. K.; Fuoss, P. H.; Stephenson, G. B.; Thompson, C.; Kim, D. M.; Choi, K. J.; Eom, C. B.; *et al.* Stabilization of Monodomain Polarization in Ultrathin $PbTiO_3$ Films. *Phys. Rev. Lett.* **2006**, *96*, 127601.
30. Wang, R. V.; Fong, D. D.; Jiang, F.; Highland, M. J.; Fuoss, P. H.; Thompson, C.; Kolpak, A. M.; Eastman, J. A.; Streiffer, S. K.; Rappe, A. M.; *et al.* Reversible Chemical Switching of a Ferroelectric Film. *Phys. Rev. Lett.* **2009**, *102*, 047601.
31. Shin, J.; Nascimento, V. B.; Geneste, G.; Rundgren, J.; Plummer, E. W.; Dkhil, B.; Kalinin, S. V.; Baddorf, A. P. Atomistic Screening Mechanism of Ferroelectric Surfaces: An *In Situ* Study of the Polar Phase in Ultrathin $BaTiO_3$ Films Exposed to H_2O. *Nano Lett.* **2009**, *9*, 3720–3725.
32. Dahan, D.; Molotskii, M.; Rosenman, G.; Rosenwaks, Y. Ferroelectric Domain Inversion: The Role of Humidity. *Appl. Phys. Lett.* **2006**, *89*, 152902.
33. Kholkin, A. L.; Bdikin, I. K.; Shvartsman, V. V.; Pertsev, N. A. Anomalous Polarization Inversion in Ferroelectrics *via* Scanning Force Microscopy. *Nanotechnology* **2007**, *18*, 095502.
34. Bristowe, N. C.; Littlewood, P. B.; Artacho, E. Surface Defects and Conduction in Polar Oxide Heterostructures. *Phys. Rev. B* **2011**, *83*, 205405.
35. Kalinin, S. V.; Jesse, S.; Tselev, A.; Baddorf, A. P.; Balke, N. The Role of Electrochemical Phenomena in Scanning Probe Microscopy of Ferroelectric Thin Films. *ACS Nano* **2011**, *5*, 5683–5691.
36. Bristowe, N. C.; Stengel, M.; Littlewood, P. B.; Pruneda, J. M.; Artacho, E. Electrochemical Ferroelectric Switching: Origin of Polarization Reversal in Ultrathin Films. *Phys. Rev. B* **2012**, *85*, 024106.
37. Nguyen, T. L.; Dokiya, M.; Wang, S. R.; Tagawa, H.; Hashimoto, T. The Effect of Oxygen Vacancy on the Oxide Ion Mobility in $LaAlO_3$-Based Oxides. *Solid State Ionics* **2000**, *130*, 229–241.
38. Wagner, S. F.; Menesklou, W.; Schneider, T.; Ivers-Tiffee, E. Kinetics of Oxygen Incorporation into $SrTiO_3$ Investigated by Frequency-Domain Analysis. *J. Electroceram.* **2004**, *13*, 645–651.
39. Merkle, R.; Maier, J. How Is Oxygen Incorporated Into Oxides? A Comprehensive Kinetic Study of a Simple Solid-State Reaction with $SrTiO_3$ as a Model Material. *Angew. Chem., Int. Ed.* **2008**, *47*, 3874–3894.
40. Fleig, J. Voltage-Assisted ^{18}O Tracer Incorporation into Oxides for Obtaining Shallow Diffusion Profiles and for Measuring Ionic Transference Numbers: Basic Considerations. *Phys. Chem. Chem. Phys.* **2009**, *11*, 3144–3151.
41. Opitz, A. K.; Lutz, A.; Kubicek, M.; Kubel, F.; Hutter, H.; Fleig, J. Investigation of the Oxygen Exchange Mechanism on Pt|Yttria Stabilized Zirconia at Intermediate Temperatures: Surface Path *versus* Bulk Path. *Electrochim. Acta* **2011**, *56*, 9727–9740.
42. Baiatu, T.; Waser, R.; Hardtl, K. H. DC Electrical Degradation of Perovskite-Type Titanates: A Model of the Mechanism. *J. Am. Ceram. Soc.* **1990**, *73*, 1663–1673.
43. Wang, J. L.; Trolier-McKinstry, S. Oxygen Vacancy Motion in Er-Doped Barium Strontium Titanate Thin Films. *Appl. Phys. Lett.* **2006**, *89*, 172906.
44. Jiang, W.; Noman, M.; Lu, Y. M.; Bain, J. A.; Salvador, P. A.; Skowronski, M. Mobility of Oxygen Vacancy in $SrTiO_3$ and Its Implications for Oxygen-Migration-Based Resistance Switching. *J. Appl. Phys.* **2011**, *110*, 034509.
45. Yi, H. T.; Choi, T.; Choi, S. G.; Oh, Y. S.; Cheong, S. W. Mechanism of the Switchable Photovoltaic Effect in Ferroelectric $BiFeO_3$. *Adv. Mater.* **2011**, *23*, 3403.
46. Lee, D.; Baek, S. H.; Kim, T. H.; Yoon, J. G.; Folkman, C. M.; Eom, C. B.; Noh, T. W. Polarity Control of Carrier Injection at Ferroelectric/Metal Interfaces for Electrically Switchable Diode and Photovoltaic Effects. *Phys. Rev. B* **2011**, *84*, 125305.
47. Balke, N.; Jesse, S.; Morozovska, A. N.; Eliseev, E.; Chung, D. W.; Kim, Y.; Adamczyk, L.; Garcia, R. E.; Dudney, N.; Kalinin, S. V. Nanoscale Mapping of Ion Diffusion in a Lithium-Ion Battery Cathode. *Nat. Nanotechnol.* **2010**, *5*, 749–754.
48. Balke, N.; Jesse, S.; Kim, Y.; Adamczyk, L.; Tselev, A.; Ivanov, I. N.; Dudney, N. J.; Kalinin, S. V. Real Space Mapping of Li-Ion Transport in Amorphous Si Anodes with Nanometer Resolution. *Nano Lett.* **2010**, *10*, 3420–3425.
49. Kumar, A.; Ciucci, F.; Morozovska, A. N.; Kalinin, S. V.; Jesse, S. Measuring Oxygen Reduction/Evolution Reactions on the Nanoscale. *Nat. Chem.* **2011**, *3*, 707–713.
50. Morozovska, A. N.; Eliseev, E. A.; Kalinin, S. V. Electromechanical Probing of Ionic Currents in Energy Storage Materials. *Appl. Phys. Lett.* **2010**, *96*, 222906.
51. Morozovska, A. N.; Eliseev, E. A.; Balke, N.; Kalinin, S. V. Local Probing of Ionic Diffusion by Electrochemical Strain Microscopy: Spatial Resolution and Signal Formation Mechanisms. *J. Appl. Phys.* **2010**, *108*, 053712.
52. Morozovska, A. N.; Eliseev, E. A.; Svechnikov, G. S.; Kalinin, S. V. Nanoscale Electromechanics of Paraelectric Materials

with Mobile Charges: Size Effects and Nonlinearity of Electromechanical Response of $SrTiO_3$ Films. *Phys. Rev. B* **2011**, *84*, 045402.
53. Morozovska, A. N.; Eliseev, E. A.; Tagantsev, A. K.; Bravina, S. L.; Chen, L. Q.; Kalinin, S. V. Thermodynamics of Electromechanically Coupled Mixed Ionic-Electronic Conductors: Deformation Potential, Vegard Strains, and Flexoelectric Effect. *Phys. Rev. B* **2011**, *83*, 195313.
54. Kumar, A.; Ovchinnikov, O. S.; Funakubo, H.; Jesse, S.; Kalinin, S. V. Real-Space Mapping of Dynamic Phenomena during Hysteresis Loop Measurements: Dynamic Switching Spectroscopy Piezoresponse Force Microscopy. *Appl. Phys. Lett.* **2011**, *98*, 202903.
55. Guo, S.; Jesse, S.; Kalnaus, S.; Balke, N.; Daniel, C.; Kalinin, S. V. Direct Mapping of Ion Diffusion Times on $LiCoO_2$ Surfaces with Nanometer Resolution. *J. Electrochem. Soc.* **2011**, *158*, A982–A990.
56. Bark, C. W.; Sharma, P.; Baek, S. H.; Lee, S.; Ryu, S.; Folkman, C. M.; Tsymbal, E. Y.; Rzchowski, M. S.; Gruverman, A.; Eom, C. B. Switchable Induced Polarization in $LaAlO_3/SrTiO_3$ Heterostructures. *Nano Lett.* **2012**, *12*, 1765–1771.
57. Jesse, S.; Kalinin, S. V.; Proksch, R.; Baddorf, A. P.; Rodriguez, B. J. The Band Excitation Method in Scanning Probe Microscopy for Rapid Mapping of Energy Dissipation on the Nanoscale. *Nanotechnology* **2007**, *18*, 435503.
58. Jesse, S.; Guo, S.; Kumar, A.; Rodriguez, B. J.; Proksch, R.; Kalinin, S. V. Resolution Theory, and Static and Frequency-Dependent Cross-Talk in Piezoresponse Force Microscopy. *Nanotechnology* **2010**, *21*, 405703.
59. Guo, S.; Ovchinnikov, O. S.; Curtis, M. E.; Johnson, M. B.; Jesse, S.; Kalinin, S. V. Spatially Resolved Probing of Preisach Density in Polycrystalline Ferroelectric Thin Films. *J. Appl. Phys.* **2010**, *108*, 084103.
60. Jesse, S.; Kalinin, S. V. Principal Component and Spatial Correlation Analysis of Spectroscopic-Imaging Data in Scanning Probe Microscopy. *Nanotechnology* **2009**, *20*, 085714.
61. Bonnet, N. Some Trends in Microscope Image Processing. *Micron* **2004**, *35*, 635–653.
62. Bonnet, N. Multivariate Statistical Methods for the Analysis of Microscope Image Series: Applications in Materials Science. *J. Microsc.* **1998**, *190*, 2–18.
63. Bosman, M.; Watanabe, M.; Alexander, D. T. L.; Keast, V. J. Mapping Chemical and Bonding Information Using Multivariate Analysis of Electron Energy-Loss Spectrum Images. *Ultramicroscopy* **2006**, *106*, 1024–1032.
64. Stengel, M.; Vanderbilt, D. Berry-Phase Theory of Polar Discontinuities at Oxide−Oxide Interfaces. *Phys. Rev. B* **2009**, *80*, 241103.
65. Singh-Bhalla, G.; Bell, C.; Ravichandran, J.; Siemons, W.; Hikita, Y.; Salahuddin, S.; Hebard, A. F.; Hwang, H. Y.; Ramesh, R. Built-In and Induced Polarization Across $LaAlO_3/SrTiO_3$ Heterojunctions. *Nat. Phys.* **2011**, *7*, 80–86.
66. Cancellieri, C.; Fontaine, D.; Gariglio, S.; Reyren, N.; Caviglia, A. D.; Fete, A.; Leake, S. J.; Pauli, S. A.; Willmott, P. R.; Stengel, M.; *et al.* Electrostriction at the $LaAlO_3/SrTiO_3$ Interface. *Phys. Rev. Lett.* **2011**, *107*, 056102.
67. Highland, M. J.; Fister, T. T.; Fong, D. D.; Fuoss, P. H.; Thompson, C.; Eastman, J. A.; Streiffer, S. K.; Stephenson, G. B. Equilibrium Polarization of Ultrathin $PbTiO_3$ with Surface Compensation Controlled by Oxygen Partial Pressure. *Phys. Rev. Lett.* **2011**, *107*, 187602.
68. Stephenson, G. B. Highland, M. J. Equilibrium and Stability of Polarization in Ultrathin Ferroelectric Films with Ionic Surface Compensation. *Phys. Rev. B* **2011**, *84*, 064107.
69. Garcia, R.; Losilla, N. S.; Martinez, J.; Martinez, R. V.; Palomares, F. J.; Huttel, Y.; Calvaresi, M.; Zerbetto, F. Nanopatterning of Carbonaceous Structures by Field-Induced Carbon Dioxide Splitting with a Force Microscope. *Appl. Phys. Lett.* **2010**, *96*, 143110.
70. Woicik, J. C.; Li, H.; Zschack, P.; Karapetrova, E.; Ryan, P.; Ashman, C. R.; Hellberg, C. S. Anomalous Lattice Expansion of Coherently Strained $SrTiO_3$ Thin Films Grown on Si(001) by Kinetically Controlled Sequential Deposition. *Phys. Rev. B* **2006**, *73*, 024112.
71. Geneste, G.; Dkhil, B. Adsorption and Dissociation of H_2O on In-Plane-Polarized $BaTiO_3$ (001) Surfaces and Their Relation to Ferroelectricity. *Phys. Rev. B* **2009**, *79*, 235420.